13th International Symposium on Particle Image Velocimetry – ISPIV 2019
Munich, Germany, July 22-24, 2019

Experimental identification of the aerodynamic mechanisms of load reduction in a tailored flow field

Tom T. B. Wester[1*], Gerrit Kampers[1], Michael Hölling[1], Ulrike Cordes[2], Cameron D. Tropea[2], Joachim Peinke[1] and Gerd Gülker[1]

[1] ForWind - Institute of Physics, University of Oldenburg, 26111 Oldenburg, Germany

[2] Institute of Fluid Mechanics and Aerodynamics,Technical University of Darmstadt, 64287 Darmstadt, Germany

[*] tom.wester@uni-oldenburg.de

Abstract

The present study shows investigations of an airfoil equipped with a load mitigating mechanism under tailored inflow conditions in a wind tunnel. Offshore measurements taken at the FINO platform are used as a model for the generated flow field close to reality. To generate such tailored inflow with focus on angle of attack variations an active grid is used.
The aim of the study is to find major differences of the flow around a Clark-Y airfoil with an adaptive camber mechanism (ACP) compared to the baseline airfoil. In order to achieve this, the aerodynamic forces resulting from the inflow as well as the flow field are measured with temporally highly resolved force sensors and stereoscopic PIV. During the evaluation the forces are linked to the measured flow structures. Also events where the load mitigation fails and higher loads are induced were identified. To find the limits the airfoil needs to be operated beyond the linear region of the polar. Therefore, the airfoil is operated near the stall region during the experiments.

1 Introduction

In free field operation wind energy converters (WEC) face unsteady flow conditions. For example the incoming wind speed varies over a wide range of magnitude on different time scales. Those changes in the inflow velocity translate to a rapid change in the angle of attack α for the rotating blade up to several degrees in a fraction of a second. Changing the angle of attack will directly result in fluctuating aerodynamic forces and correspond to dynamic loads. Constantly varying loads cause material fatigue and a reduction of lifetime of the turbines (Spinato et al. (2009)). These problems will become even more important with the upscaling of the rotor diameter in the future. Hence, it is necessary to alleviate dynamic forces caused by turbulent inflow to reduce costs of maintenance and thereby increase the competitiveness of wind power.
A very promising approach to reduce load fluctuations is the adaptive camber profile (ACP) developed by Lambie (Lambie (2011)). This passive adaptive Clark-Y shaped airfoil changes its camber depending on the pressure difference between pressure and suction side at the airfoil leading edge. The leading and trailing edge are coupled by a spring mechanism. The spring attempts to maintain the shape into the fully cambered position and acts against the lower pressure on the suction side. This concept has been proven to decrease the slope of the polar in the linear region. By this lower slope the lift does not change much with changes of angle of attack (Lambie (2011)). In recent wind tunnel experiments a dynamic load reduction has been demonstrated for periodic sinusoidal angle of attack variations (Cordes et al. (2015, 2018)) and mexican hat shaped variations, which mimic a typical tower passing (Wester et al. (2018)). In Kampers et al. (2015) the influence of turbulent inflow on the load mitigation was investigated and confirmed for a geometric angle of attack of $\alpha_{geo} = 8^{\circ}$. This is why this angle is also chosen in the present study.
The following study expands the investigations of the aerodynamic response of the adaptive camber airfoil from rather simple periodic inflow towards realistic inflows. Realistic or turbulent inflow in this case means rapid variations in the angle of attack over several degrees on time scales below 0.1 s. Compared to periodic

flows, these time scales and the amplitudes are not constant. This means that different magnitudes of angle of attack variations over different time scales occur.

2 Experimental Setup

The experiments are performed with the same setup, as presented by Wester et al. (2018). A schematic sketch of the setup is shown in figure 1. The wind tunnel is a Göttingen type wind tunnel with an nozzle of (0.8×1.0) m^2 $(H \times W)$ and a 2.6 m long closed test section. The wind speed during the measurements is kept at $14\frac{m}{s}$. To tailor the flow a 2D active grid is used. The grid is attached to the outlet nozzle of the wind tunnel and consists of nine individual movable shafts. These shafts are flat plates with a chord length of 90 mm and a span of 0.8 m to cover the whole height of the outlet. This setup also ensures a homogeneous AoA change along the span of the airfoil. The movement of the shafts is actuated with a control protocol which contains information about the movement of each shaft of the grid. Furthermore, the predefined motion of the shafts enables repeatable measurements of different airfoils under comparable varying inflow conditions over time. To ensure that the flow has the desired changes in angle of attack over time, temporally highly resolved X-wire measurements had been performed beforehand. The measurements were performed with a sampling frequency of $f_{s,XW} = 20$ kHz at the intended leading edge position of the airfoil. During those measurements the wind tunnel was empty. The measurement system was a *StreamLine* from *Dantec Dynamics* with a 55*P*61 Probe.
During the experiments a Clark-Y airfoil with a chord of $c = 0.185$ m and a span of $s = 0.8$ m was used, resulting in a chord based Reynolds number of $Re_c = 175 \times 10^3$. The geometric AoA of the airfoil is kept constant at $\alpha_{geo} = 8°$. The resulting AoA for the airfoil is the sum of α_{geo} and the generated angle of the inflow $\phi(t)$. In the following the airfoil with the adaptive camber mechanism is referred to as "flexible" and the baseline airfoil as "rigid". The airfoil itself is mounted vertical in the test section 1.1 m downstream of the grid at its quarter point. By this gravitational forces can be neglected while measuring drag and lift.
The global acting forces are measured with two force balances of type *K3D120* and a torque sensor of type *TS110* from *ME-Messsysteme*. The sensors are mounted on the shaft outside of the measurement section. To investigate the flow in more detail, stereoscopic PIV measurements on the suction side of the airfoil are performed. The system consists of two *Phantom Miro 320S* cameras with 12GB of RAM and a *Litron 303HE* Laser which is operated at a repetition rate of $f_{s,PIV} = 500$ Hz. The resolution of the cameras was adapted to (1664×944) px ^{2} to be able to measure 5.2 s resulting in 2600 frames. The resulting field of view has a size of (440×260) mm^2 with a spatial resolution of (1.12×1.12) mm^2. All measurement systems and the active grid are triggered to guarantee synchrony during the measurements.

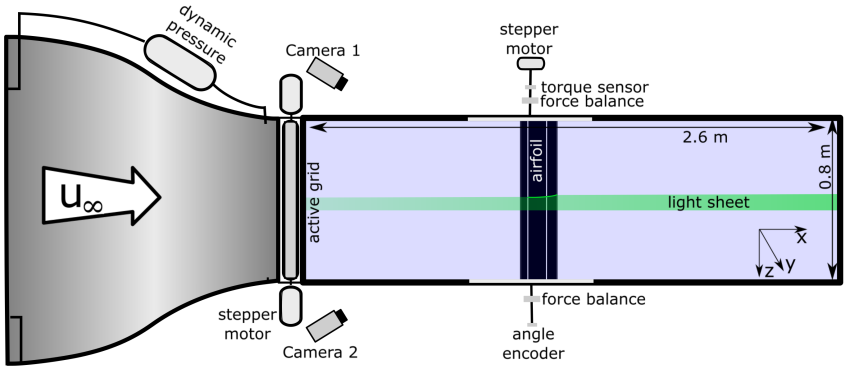

Figure 1: Side view of the wind tunnel with closed test section, active grid, force balances and PIV setup (Wester et al. (2018)).

3 Results

3.1 Inflow

Before the aerodynamic effects can be interpreted in detail it is necessary to examine the inflow generated by the active grid. During the experiments it needs to be distinguished between the angle of inflow ϕ which is generated by the active grid, the geometric angle of attack α_{geo} the airfoil has and the angle of attack α which is the sum of ϕ and α_{geo}. Figure 2 shows a representative cutout of the angle of inflow variations ϕ generated by the grid and measured with a X-wire and PIV in the empty measurement section. The data are extracted from the intended leading edge position. The entire generated time series is 60 s long. Since the main flow velocity is nearly constant, the u_x component of the flow will not contribute to the later observed effects and the focus lies on the ϕ variations.

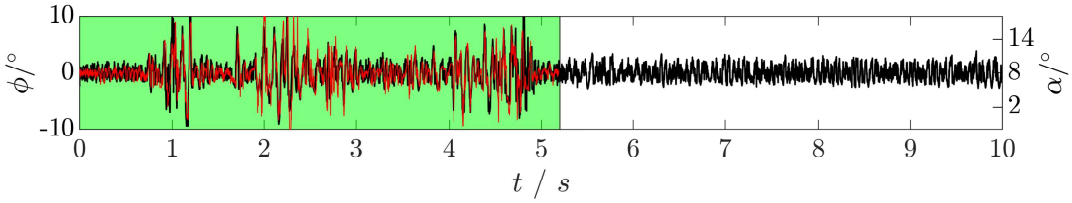

Figure 2: Left y-axis: Measured angle of inflow $\phi(t)$ from X-wire in black and PIV in red. The underlying green background represents the time of the PIV measurements. The right y-axis shows the resulting angle of attack $\alpha(t)$ variation for the airfoil.

The generated inflow has a mean of $\overline{\phi(t)} = 0°$ and a standard deviation of $\sigma_\phi = 1.7°$. The comparison of the PIV measurement of the empty wind tunnel shown in red and the underlying X-wire measurements in black shows a very good agreement, which underlines the reproducibility of the generated inflow since the measurements have not been performed simultaneously. Small deviations between both time series can be explained by the nature of turbulence which cannot be controlled.
To obtain better insight into the generated flow structures figure 3 shows a spectrum of the inflow. Here the energy is plotted over the reduced frequency $k = \frac{\pi \cdot c \cdot f}{u}$. The spectrum shows a broad peak from $k = 0.2$ up to $k = 3$. This peak represents the energy the grid imprints onto the inflow. For values of $k > 0.2$, a flow is said to be highly unsteady (Leishman (2006)). Since the main energy is added for reduced frequencies above this threshold the generated inflow is highly unsteady. Such flows are changing faster than the airfoil aerodynamics can react. As a result, effects such as dynamic stall are triggered. These reduced frequencies are related to length scales of 0.19 m to 2.8 m. Since this corresponds to the size of the airfoil, these events will influence the generated lift and the aerodynamics directly.

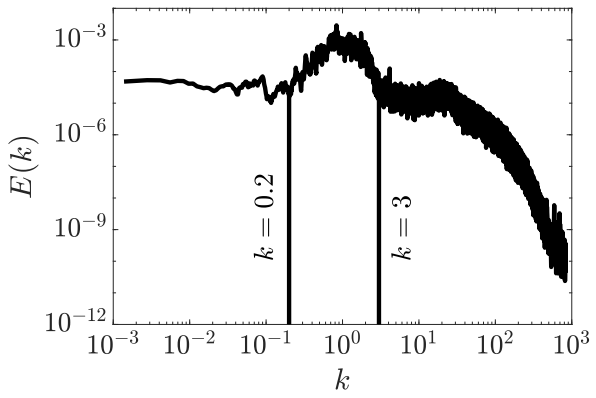

Figure 3: Energy spectrum of the generated angle of attack fluctuations.

3.2 Forces and ACP Mechanism

After characterizing the inflow the generated lift will be investigated and compared for both airfoils. During the 60 s force measurement the rigid airfoil generates a mean lift of $\overline{C_{L,rigid}} = 0.60 \pm 0.13$ whereas the flexible one reaches $\overline{C_{L,flexible}} = 0.74 \pm 0.12$ at the mean geometric AoA $\alpha_{geo} = 8°$. This means that the mean lift is increased by 23% and in addition the standard deviation is also reduced by nearly 10%. This underlines the findings from the previous studies and extends this to more complex flows.
Figure 4 shows a cutout of the time series of the lift coefficient C_L over time. The time series indicates events in the lift time series in which the flexible airfoil has larger variations than the fixed one. This underlines the fact that the one point statistic of mean and standard deviation is not able to capture any kind of temporal effects. To compare the real effectiveness of the ACP such effects also need to be taken into account. By this the performance of the ACP can be improved further and it can be identified under what conditions the airfoil fails to damp the lift fluctuations. Hence, the lift time series is investigated regarding events where the lift fluctuations of the ACP are higher compared to the rigid airfoil. For identifying such events a local standard deviation is calculated in moving bins of 0.1s. If this local standard deviation of the ACP is higher compared to the standard deviation of the rigid airfoil this is defined as "critical behavior". Those events are marked with a red background in figure 4. For the given inflow during 35% of the time such cases occur. Comparing figure 4 with figure 2 the times of critical behavior seem to occur more often during large variations of ϕ. Since the moving leading and trailing edge flaps are the main difference between both airfoils, they must cause the different lift response. For this reason the reaction of the trailing edge to the inflow will be investigated.

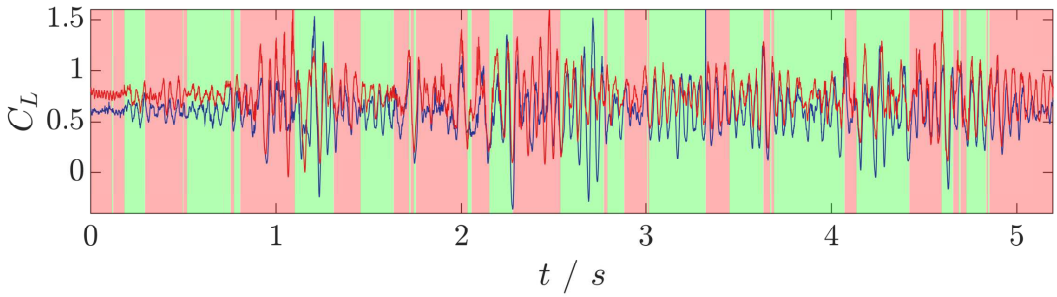

Figure 4: Extract from measured lift coefficient for the rigid airfoil in blue and flexible ACP in red. Background color represents the state of the system where red denotes a critical behavior and green fluctuation reduction.

Figure 5(a) focuses on a cutout where a critical behavior occurs. The plot shows in red the reaction of the trailing edge flap (TEF) by angle β to the changing α shown in black. A positive β denotes a decambering and negative β a cambering of the airfoil. $\beta = 0°$ corresponds to the normal Clark-Y shape. During the measurement the mean angle is $\overline{\beta} = -1.3°$. This explains the higher overall mean lift force of the ACP, since a higher camber generates higher lift. Comparing the inflow with β, mainly a decambering for an increase of ϕ and a cambering for decreasing ϕ can be observed. This is the expected behavior, because an increase of AoA leads to higher lift and therefore a decambering of the airfoil counteracts this increase and vice versa. More interesting is the obvious time lag between inflow and reaction of the TEF, which can be observed in figure 5(a). From correlating ϕ and β an average response time of (0.039 ± 0.003) s can be derived. This corresponds at the given wind speed to a convection length of 0.55 ± 0.04 m, which is three times the chord of the airfoil. Compared to this the lift response in figure 5(b), where the lift fluctuations $\Delta C_L(t) = C_L(t) - \overline{C_L}$ is plotted over time, shows a delay of only (0.016 ± 0.002) s, corresponding to a distance of 0.22 ± 0.03 m for the given wind speed. This is a little above the contraction time of the flow over the chord. Since the pressure difference and therefore the lift is the driving force of the ACP mechanism, this delay between inflow, resulting lift and trailing edge flap is the limiting time constant for this system. If the inflow changes faster than the flap is able to react the system is driven into a state where extreme lift dynamics can be amplified. Examples of such amplifications are marked with numbers $(1-3)$ in figure 5(a) for inflow and resulting TEF reaction and in figure 5(b) for the resulting lift.
The first event (1) shows a negative β, which means the airfoil is cambered. At the same time ϕ reaches a local maximum resulting in an overshoot in lift compared to the rigid airfoil. The exact opposite happens at (2), where the airfoil is decambered ($\beta > 0$), even though ϕ is at a local minimum. This leads to a massive dip

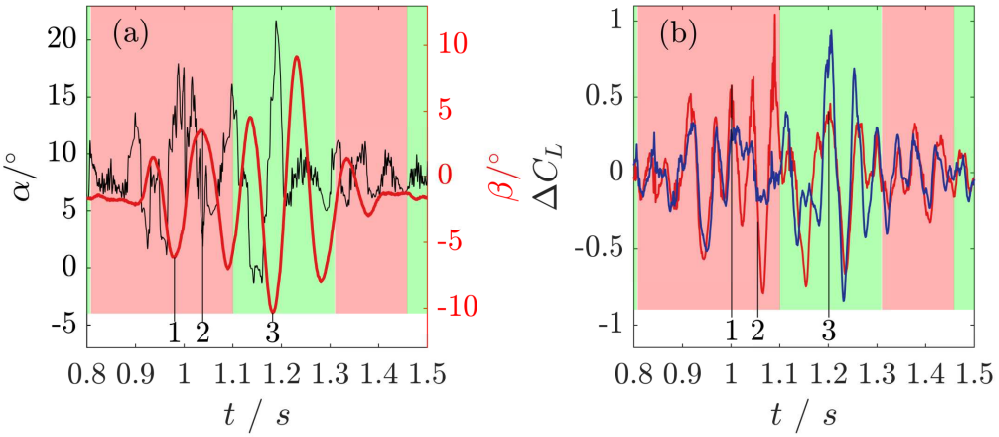

Figure 5: (a) shows the inflow in black together with the TEF response in red. (b) shows the resulting lift coefficient for the flexible airfoil in red and the rigid one in blue. The red background in both figures represents a critical behavior like in figure 4. The numbers mark the chosen events.

in the generated lift, which than again triggers a cambering of the airfoil leading to an even higher overshoot of the lift. This behavior repeats itself and the amplitude of β increases with every repetition. In the given example this culminates in situation (3) with a 180° phase shift between inflow and TEF. Interestingly, this should also result in an even higher lift overshoot, but in this situation the lift response is damped rather than increased. To obtain insight into, what effects cause this behavior, all this three occurring situations will be investigated with PIV in the following section.

4 Particle Image Velocimetry

4.1 Vector fields

After identifying events where the ACP amplifies the lift fluctuations the flow field around both airfoils needs to be compared. Figure 6 shows the normalized u_x component of the flow around the airfoils during the event (1) in figure 5. The left hand side of the figure shows the rigid airfoil and the right side the flexible airfoil. For comparison the original position of leading and trailing edge flaps are added as a red outline on the flexible airfoil. In this case the downwards deflected trailing edge flap leads to a higher cambering and therefore to an increase of the flow velocity at the thickest point of the airfoil ($\frac{x}{c} \approx 0.25$). By this a higher lift compared to the rigid airfoil is generated. This agrees with the findings in figure 5 (b).

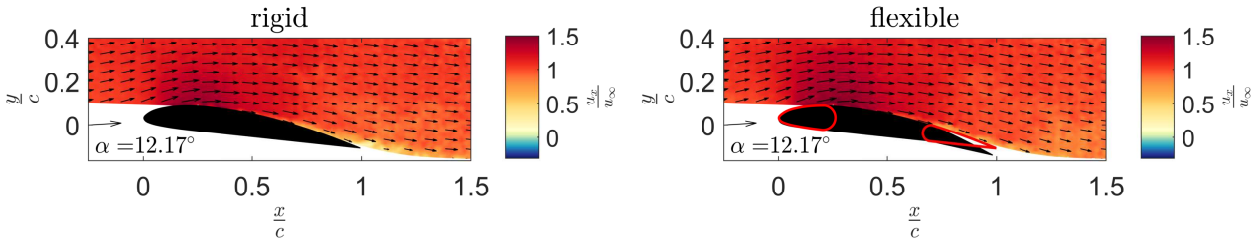

Figure 6: Normalized u_x component of the flow around the rigid and flexible airfoil during event (1).

A consequence of the higher cambering is shown in figure 7, where the flow 0.02 s after event (1) is shown. The flap is already moving towards the zero position. At the back part of both airfoils an increase of the shear layer thickness from trailing edge towards leading edge can be observed. This is indicated by the low

velocity wake which occurs for $\frac{x}{c} \approx 0.6$. For the flexible airfoil the velocity deficit is larger and the wake is slightly wider. This reinforced thickening of the shear layer compared to the fixed airfoil initiates the dip in the lift curve right after the lift peak. The ongoing decambering leads to situation (2) in figure 5 and is

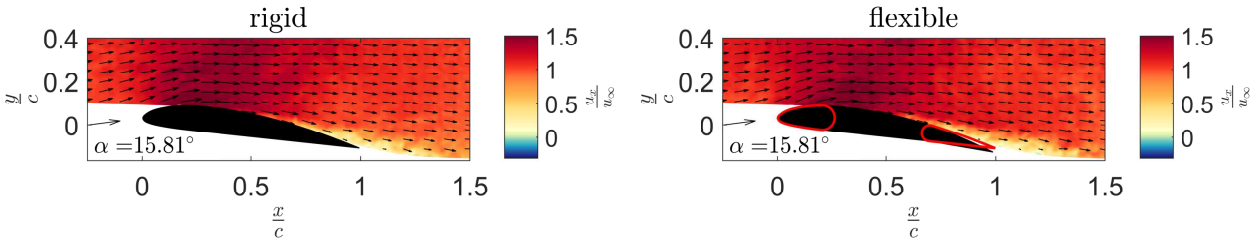

Figure 7: Normalized u_x component 0.02 s after the high cambering during situation (1).

shown in figure 8. The flexible airfoil reacts to a higher lift with decambering. The upwards deflected TEF results in an upwards deflected airfoil wake. This reduces the lift and by the movement a vortex is shed at the trailing edge 0.012 s after situation (2). The vortex is shown in figure 9.

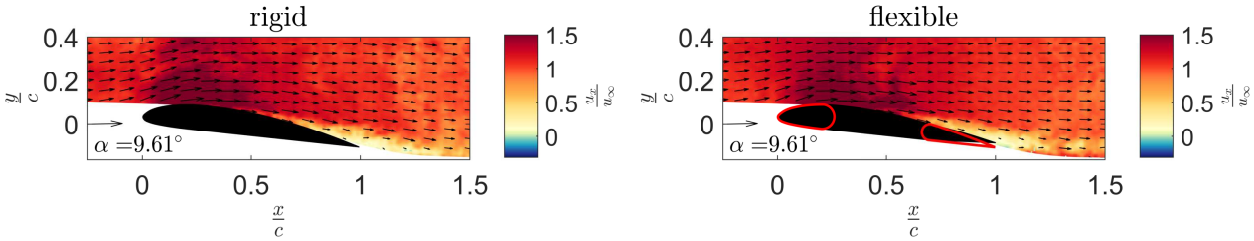

Figure 8: Normalized u_x component of the flow around the rigid and flexible airfoil during event (2).

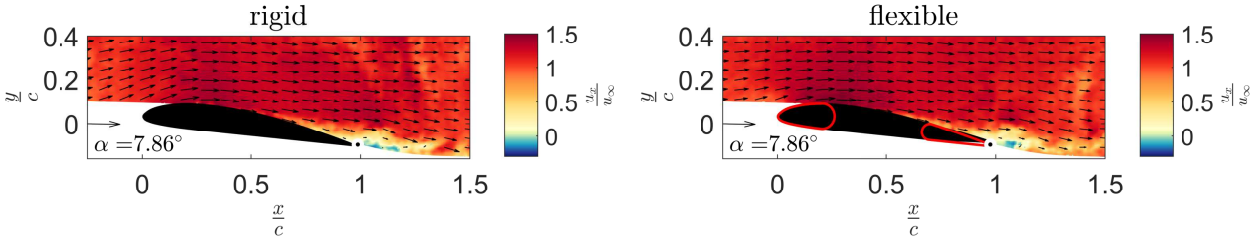

Figure 9: Normalized u_x component 0.012 s after the upwards deflection of the TEF during situation (2). The white circle near the trailing edge represents the flow separation point.

In addition the rigid airfoil shows a back flow beginning at the trailing edge of the airfoil during this situation. This is in agreement with the reduction of lift for the airfoil. The flexible airfoil also shows this back flow at the trailing edge, but due to the upwards movement of the flap this results in the mentioned vortex. This vortex is the reason for the massive dip in lift occurring immediately after situation (2) in figure 5. In the figure also the point of separation is shown as a white circle close to the trailing edge of the airfoils. For both airfoils the separation occurs near the trailing edge at comparable positions. During the last event a similar behavior compared to situation (1) would be expected, because the TEF is deflected downwards while the AoA is increased. Therefore, also here a lift overshoot is expected. The resulting flow field is shown in figure 10. Here also an increase of the flow velocity on the suction side of the airfoil can be found.

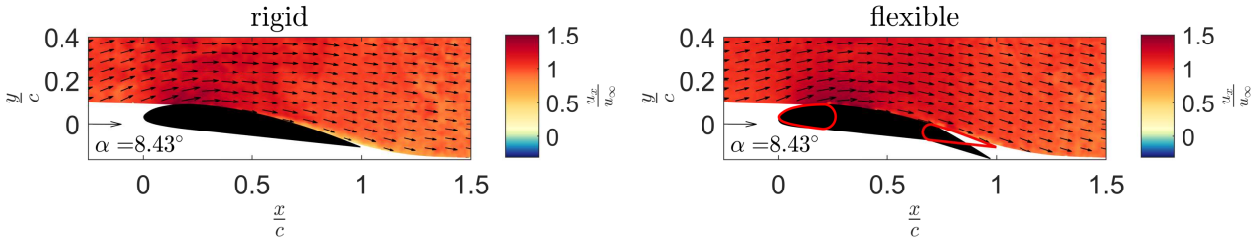

Figure 10: Normalized u_x component of the flow around the rigid and flexible airfoil during event (3).

This is in agreement with situation (1). The main difference is the reaction of the flow after the cambering, which is shown in figure 11. For the rigid airfoil the flow stays attached, resulting in the lift peak shown in figure 5. In contrast to this the flexible airfoil shows a massive flow separation at the trailing edge. This flow separation reduces the generated lift compared to the attached rigid airfoil. This reduction of lift leads during this situation to a stop of a further increasing lift and therefore a reduction of lift fluctuation compared to the rigid airfoil. This last situation shows how fast the whole flow situation can change when the starting condi-

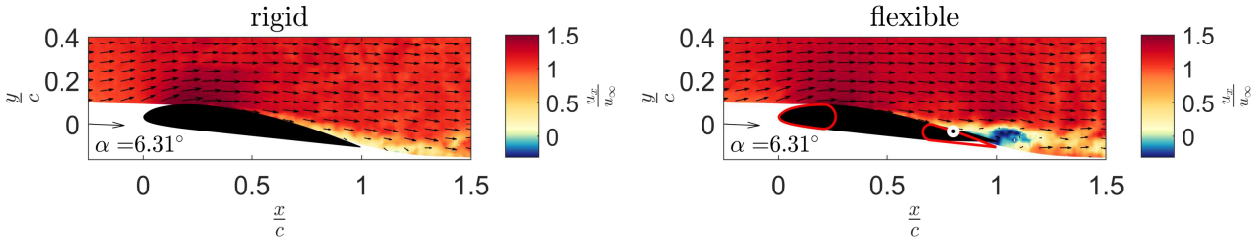

Figure 11: Normalized u_x component of the flow around the rigid and flexible airfoil 0.03 s after event (3). The white circle represents the flow separation point.

tions differ only slightly. Just because the flap is deflected a little more downwards and the AoA increases a little faster than during event (1) the mechanism which has increased the lift fluctuations starts to damp the fluctuations like it was intended. Overall this last event shows that even if there are situations when the ACP mechanism is inhibited by its time delay, exactly this delay can lead to a damping of lift fluctuations in complex flow situations.

4.2 Proper Orthogonal Decomposition

Besides the plain interpretation of the velocity fields in this section also the coherent structures should be identified using the proper orthogonal decomposition (POD), which was already used in Sirovich (1987). By using this approach the very complex aerodynamics can be reduced in complexity, because the complete flow field is separated into its eigenmodes (λ_i) with their time coefficient ($a_i(t)$). The eigenmodes are sorted by the energy they contain and therefore by their influence on the flow field. This means that the first modes represent the major coherent structures which most affect the flow.
Since the first mode of the POD is the mean field, the mean is subtracted before calculating the POD. By this just the fluctuations are investigated. The number of eigenmodes is always equal to the number of images used to calculate the POD. Furhtermore, the velocity field v at time t can be fully reconstructed by multiplying each mode with its time coefficient (a_i) and adding all modes up to the mean field $\overline{v}$ (see equation 1). This means a_i directly reflects the importance of the mode at a given time t. Using this property it is possible to check which structures are correlated with the given inflow and which are connected to the

generated forces.

$$v(t) = \overline{v} + \sum_{i=1}^{N} a_i(t) \cdot \lambda_i \tag{1}$$

The first POD modes are shown in figure 12. For both airfoils this mode represents a separation, which forms on the suction side and also the wake of the airfoil. This mode contains 19% of the fluctuating energy for the rigid airfoil and 28% for the flexible ACP. By comparing the modes with each other, they do not seem to be really different. Both show the beginning of separation at $\frac{x}{c} = 0.55$ and that the airfoil wake is mainly emphasized when the boundary-layer separation takes place ($a_1 > 0$). On a closer look however, it becomes clear that there are small differences. The separation area of the flexible airfoil covers a larger area. This becomes clear when the extension of the wake in the airfoil normal direction is viewed at. Besides this also the influence on the flow around the airfoil is different. For the rigid airfoil the velocity increases significantly when the separation is present ($a_1 > 0$) and decreases without the separation ($a_1 < 0$). This can be seen by the red area above the airfoil. This area will give a positive proportion to the mean flow field for a positive a_1. This effect is also the case for the flexible airfoil, but only with a rather small magnitude. Since these two modes are the most energetic ones and represent a flow phenomenon which is strongly coupled to the angle of attack one would expect this modes to correlate directly with the inflow. Figure 13 (a) shows the angle of inflow ϕ compared to the time coefficients a_1. Both coefficients show the same trend as the α

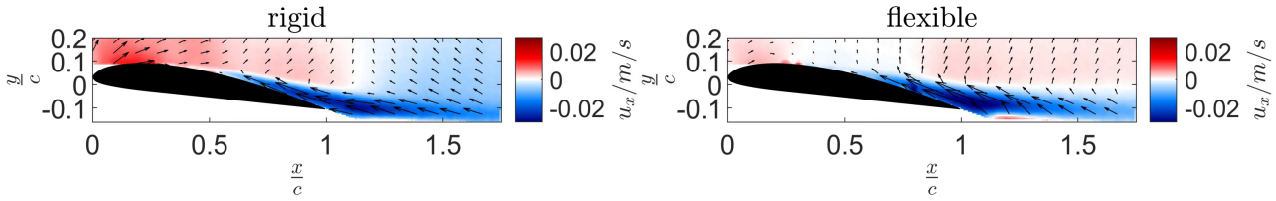

Figure 12: First POD mode for the rigid airfoil on the left and flexible ACP on the right hand side.

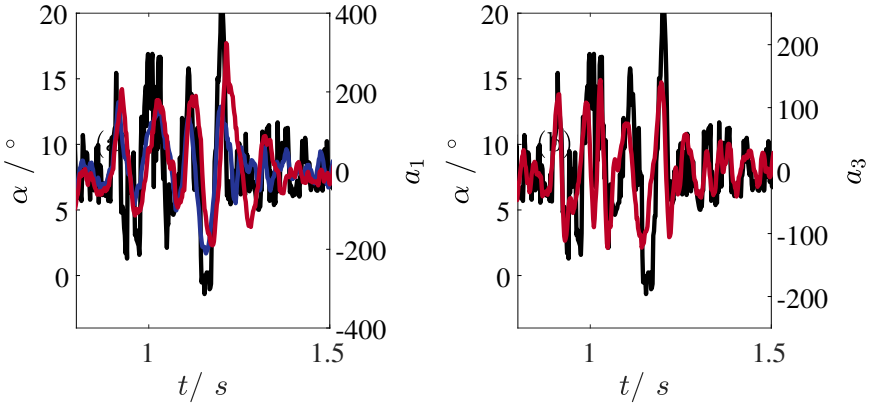

Figure 13: (a) time coefficients in blue for the rigid and in red for the flexible airfoil of the first POD Mode compared to the AoA in black. (b) third time coefficient for the flexible airfoil (red) compared to the AoA (black).

variation. This means a direct correlation between the inflow and the flow separation. Interestingly, for the rigid airfoil this first mode is the one which is strongest correlated to the inflow with a correlation coefficient of $\rho = 67\%$. For the flexible airfoil in turn this first mode is surprisingly not the one most strongly correlated with the inflow. Here the inflow is more correlated with the third mode, as shown in figure 14, which contains only 7% of the energy. This mode correlates with the inflow with a correlation coefficient of $\rho = 58\%$.

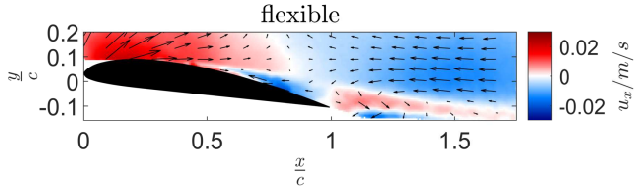

Figure 14: Third POD mode for the flexible airfoil.

The first mode only has the second highest correlation with $\rho = 42\%$. This third mode represents mainly the flow in the wake region, as well as an decreasing flow velocity near the trailing edge. This corresponds to the movement of the flap, because with an increase of α the flap also moves upwards resulting in a decrease of the flow velocity. In addition to this slowing down, the wake of the airfoil is deflected upwards. So the third mode of the POD is here directly representing the movement of the trailing edge flap. Since this movement is caused by the changing AoA it becomes quite clear why this mode is so strongly correlated to the inflow. Furthermore, the increase of velocity at the thickest point of the airfoil is comparable to the structure found in the first mode of the rigid airfoil. Figure 13 (b) shows the time coefficient of the third mode compared to the inflow. By comparing the first and third coefficient it is obvious that the modes are mainly occurring simultaneously.
Another goal is to find the POD modes representing the lift fluctuations. A first guess would be that the modes correlated to the inflow are also the ones most correlated to the acting forces. By comparing the correlation coefficients this conjecture is also confirmed. For the rigid airfoil again, the first and most energetic POD mode exhibits the highest correlation. This can be easily explained, because the speed-up and slowing down of the flow represented by this mode is the main effect generating a lift force. Compared to this, the flexible airfoil again shows a deviation from the assumptions. Although the third mode is also strongly correlated with the forces, there is a second mode, which is just as strongly related to the generated lift. The fourth mode with 5% energy shown in figure 15 seems to be equally important for the generated lift as the third one. That those modes play together is easy to recognize. The fourth mode is also directly linked to the movement of the flap and thus the curvature of the profile. It is also immediately clear that this mode contributes greatly to the lift, because it reflects significantly the flow velocity on the suction side of the airfoil again.

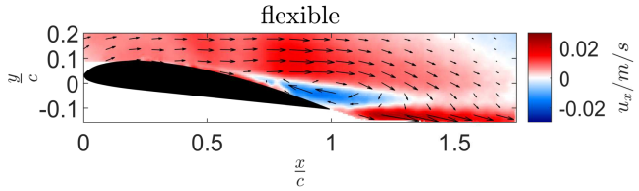

Figure 15: Fourth POD mode for the flexible airfoil.

5 Summary

In this study it could be shown that the ACP is able to reduce mean lift fluctuations for complex inflows. Even for very fast changing angles of attack the load mitigation principle works and a reduction of standard deviation could be measured. This reduction of fluctuations leads to reduced fatigue loads compared to normal airfoils without an ACP mechanism. These results underline the high potential of the ACP. Furthermore, the airfoil also increases the mean generated lift, which is a huge advantage considering the increase of power output for a wind energy turbine.
Beside the mentioned benefits also drawbacks of the mechanism could be identified. The biggest problem of the mechanism is the spring and the inertia causing a temporal delay between inflow and cambering. This

time delay could be identified and quantified during the experiments and it could be shown that this delay causes phase shifts between inflow and the flap reaction, resulting in an amplification of dynamic loads. To overcome such amplifications the response time of the mechanism needs to be reduced to a minimum.
The PIV measurements also revealed that for certain events the delay of the flap improves the lift response, because the phase shifted cambering enforces a flow separation and therefore a stop of lift overshooting compared to the baseline airfoil. Furthermore, the PIV data could be used for a POD. By correlating the POD modes with the inflow and also to the resulting forces the most important coherent structures could be identified. Major differences in the generation of lift and also response to the given inflow were identified. It could be shown that for both airfoils the flow separation is strongly correlated with the inflow. For the flexible airfoil, the separation only plays a minor role for the generation of lift. The structures induced by the change of the profile shape play a much more important role.

Acknowledgements

The present investigations were performed within the research focus "Wind Turbine Load Control under Realistic Turbulent In-Flow Conditions", funded by the German Research Foundation (DFG), Ref.Nr. PE 478/15-2 and TR 194/51-2. The authors gratefully acknowledge the DFG for funding the studies. We also acknowledge A. Abdulrazek, A. Fuchs and D. Traphan for helpful discussions.

References

Cordes U, Hufnagel K, Tropea CD, Kampers G, Hölling M, and Peinke J (2015) Experimental investigation of passive load reduction under dynamic inflow conditions. in *33rd AIAA Applied Aerodynamics Conference*. page 3313

Cordes U, Lambie B, Hufnagel K, Spiegelberg H, Kampers G, and Tropea C (2018) The adaptive camber concepta passive approach for gust load alleviation on wind turbines. *Wind Energy* 21:732744

Kampers G, Cordes U, Tropea CD, Hoelling M, and Peinke J (2015) Stochastic analysis of aerodynamic forces acting on a self-adaptive camber airfoil in turbulent inflow. in *33rd AIAA Applied Aerodynamics Conference*. page 2427

Lambie B (2011) *Aeroelastic investigation of a wind turbine airfoil with self-adaptive camber*. Ph.D. thesis. Technische Universität Darmstadt

Leishman GJ (2006) *Principles of Helicopter Aerodynamics*. Cambridge University Press, New York. 2nd edition

Sirovich L (1987) Turbulence and the dynamics of coherent structures. *Quarterly of Applied Mathematics* 45:561–571

Spinato F, Tavner PJ, Van Bussel G, and Koutoulakos E (2009) Reliability of wind turbine subassemblies. *IET Renewable Power Generation* 3:387–401

Wester TTB, Kampers G, Gülker G, Peinke J, Cordes U, Tropea C, and Hölling M (2018) High speed piv measurements of an adaptive camber airfoil under highly gusty inflow conditions. in *Journal of Physics: Conference Series*. volume 1037. page 072007. IOP Publishing